Materials Today Advances 24 (2024) 100540

Contents lists available at ScienceDirect

Materials Today Advances

journal homepage: www.journals.elsevier.com/materials-today-advances/

High-entropy alloys as magnetic shielding materials in low-frequency wireless power transmission

Cheng-Hsien Yeh [a], Chia-Hua Hu [a], Hsuan-Ta Wu [b], Wen-Dung Hsu [c,d,e], Bernard Haochih Liu [c,e], Peter K. Liaw [f], Chuan-Feng Shih [a,e,*]

[a] *Department of Electrical Engineering, National Cheng Kung University, Tainan, 70101, Taiwan*
[b] *Department and Institute of Electrical Engineering, Minghsin University of Science and Technology, Hsinchu, 30401, Taiwan*
[c] *Department of Materials Science and Engineering, National Cheng Kung University, Tainan, 70101, Taiwan*
[d] *Program on Semiconductor Packaging and Testing, Academy of Innovative Semiconductor and Sustainable Manufacture, National Cheng Kung University, Tainan, 70101, Taiwan*
[e] *Applied High Entropy Technology (AHET) Center, National Cheng Kung University, Tainan, 70101, Taiwan*
[f] *Department of Materials Science and Engineering, The University of Tennessee, Knoxville, TN, 37996, USA*

ABSTRACT

Soft magnetic materials are required to exhibit high saturation magnetization and low coercivity. Iron-based metal alloys, such as FeMnZn, are commonly used commercial soft magnetic materials with electromagnetic shielding functions. However, these alloys generally exhibit low saturation magnetization, poor high-temperature stability, and significant magnetic losses. In recent years, many research groups have highlighted the excellent soft magnetic properties of high-entropy alloys (HEAs). This study develops new HEA powders with superior soft magnetic characteristics for applications in low-frequency magnetic shielding components. The research found that the FeCoNiSiCuNb HEA, under appropriate ball-milling and annealing conditions, exhibits high saturation magnetization and excellent high-temperature properties, retaining over 50 % of its magnetism even at 700K. At an operating frequency of 100 kHz, compared to FeMnZn, the real permeability of the FeCoNiSiCuNb HEA is increased by 2.25 times. Preparing this HEA material as a magnetic shielding material can lead to higher inductance, a coupling coefficient increased to 0.84, and a transmission efficiency improvement of 19 %, demonstrating the potential of high-entropy alloys in wireless charging applications.

1. Introduction

Ideal magnetic shielding materials should possess high magnetic permeability, high saturation magnetization, low coercive force, thermal stability, and high electrical resistivity [1–8]. Magnetic shielding materials often use soft magnetic materials [9–12], which can be categorized based on their characteristics into iron-based sintered alloys such as silicon steel and ferrites [13–16]. Iron-based alloys have the advantages of high magnetic flux density and high magnetic permeability but suffer from low resistivity, which leads to increased eddy current losses at high frequencies, thereby limiting their usage conditions [17,18]. Ferrites, on the other hand, have the advantage of high resistivity, allowing for lower eddy current losses in high-frequency operating environments [19,20]. However, the saturation magnetization of ferrites is significantly lower than that of metallic soft magnetic materials, which limits their use in high-power environments.

Since high-entropy alloys (HEAs) were first proposed in 2004, they have rapidly developed. The various properties of HEAs, such as high hardness and ductility [21–24], high-temperature stability [25,26], magnetic properties [4,27–29], electrical conductivity [30], and optical properties [31], have been widely researched. These exceptional characteristics demonstrate significant potential for various applications. Among them, HEAs based on FeCoNi demonstrate good soft magnetic properties and are abundant and cost-effective [32–35]. The addition of other elements, such as copper, chromium, and silicon can adjust their properties, improving tensile performance [36,37], strength [36–40], and corrosion resistance [38,40,41]. For example, adding a small amount of aluminum can produce nano-precipitates that increase the alloy's strength without affecting tensile ductility [36]; adding a small amount of niobium can aid in solid-solution strengthening and the formation of intermetallic compounds, thus increasing yield strength [39]; adding silicon, manganese, and molybdenum can significantly increase microhardness [40,42]. Overall, these high-entropy alloys exhibit above advantages. Compared to other HEAs, the FeCoNiSi series of high-entropy alloys have higher saturation magnetization and lower coercive force [43–46]. Additionally, it is indicated that the FeCoNiCrAl

---

[*] Corresponding author. Department of Electrical Engineering, National Cheng Kung University, Tainan, 70101, Taiwan.
E-mail address: cfshih@mail.ncku.edu.tw (C.-F. Shih).

https://doi.org/10.1016/j.mtadv.2024.100540
Received 1 August 2024; Received in revised form 23 October 2024; Accepted 1 November 2024

has soft magnetic characteristics, but its drawback is a lower saturation magnetization compared to traditional ferrites [47,48]. Another research team found that FeCoNiAlCr powders, after wet milling, exhibited better shielding performance in the Kα band compared to larger plate-like powders [49]. Studies using arc melting to produce FeCoNiSiAl have shown that increasing the silicon content effectively reduces the hysteresis loop parameter (λs) and improves resistivity, thereby decreasing eddy current losses [50,51]. Furthermore, the FeCoNiCrCu has also been reported to have excellent and temperature-stable soft magnetic properties [1].

Many electronic devices require the use of soft magnetic materials. Soft magnetic materials, which possess low coercivity, are applicable across a range of frequencies from tens of Hz to several hundred MHz [20,52,53]. For instance, they are used in low-frequency applications such as motors [54,55], high-frequency applications, including filters, and radio antennas [56,57]. However, there is scarce literature on the use of HEA powders as magnetic shielding materials in the kilohertz (KHz) range [10,58]. In this frequency range, an important application is wireless power transmission [59]. There are many methods of wireless power transmission, among which electromagnetic induction is the simplest and currently the most widely used method. However, it has the limitation of only being suitable for short-range transmission. To optimize magnetic flux coupling, the transmitting and receiving coils must be very close to each other, with the transmission distance being less than the geometric dimensions of the coils. Transformers, where the magnetic field of coils is confined within a core material with high magnetic permeability, are a typical example of energy transmission by electromagnetic induction [57,60]. Other major applications include charging devices for electric toothbrushes, radio-frequency identification (RFID) smart cards, portable electronic devices, such as laptops and mobile phones, and medical implant devices [61–63].

The present research designs FeCoNiSiCuNb HEAs for applications in the low-frequency range. The material selection includes Fe, Co, and Ni as magnetic elements, which have been proven to form a stable fcc solid solution phase [64–66]. The addition of Si reduces electrical conductivity and eddy current losses, while also enhancing the overall performance [67,68]. A small amount of Nb is added to suppress excessive grain growth and improve the mechanical strength of the material [39]. The trace addition of Cu enhances grain boundary characteristics, contributing to the high-temperature stability of the material [6,69]. It involves preparing FeCoNiSiCuNb HEA powders through a mechanical alloying method and investigating the effects of process parameters on their magnetic and electrical properties. Finally, the magnetic shielding wireless charging devices made from these HEA powders demonstrate high applicability compared to traditional soft magnetic materials.

2. Methods

2.1. Material preparation

The $Fe_{32.5}Co_{23.5}Ni_{25}Si_{15}Cu_{1}Nb_{3}$ high-entropy alloy powder is synthesized using a Planetary Mono Mill PULVERISETTE 6 (FRITSCH) by mechanical alloying. High-purity elemental powders of Fe, Co, Ni, Si, Cu, and Nb, each with a purity of 99.9 wt%, are used as raw materials. The particle sizes are controlled to ensure optimal milling conditions: Fe, Co, Si, and Cu powders are less than 45 μm, Nb powder is less than 10 μm, and Ni powder is less than 4 μm. The ball-to-powder ratio is fixed at 15:1, and the milling speed is set at 300 rpm. During the milling process, there is a 40-min milling followed by a 20-min pause to prevent overheating. The mechanical alloying involves initial dry milling (using absolute ethanol) followed by wet milling (with absolute ethanol added as a process control agent, PCA) to produce the HEA [70]. The prepared samples are named as W0 (dry milling 5 h, wet milling 0 h), W5 (dry milling 5 h, wet milling 5 h), W10 (dry milling 5 h, wet milling 10 h), W20 (dry milling 5 h, wet milling 20 h), W30 (dry milling 5 h, wet milling 30 h), D0 (dry milling 0 h, wet milling 10 h), D5 (or W10, dry milling 5 h, wet milling 10 h), D10 (dry milling 10 h, wet milling 10 h), D20 (dry milling 20 h, wet milling 10 h), and D30 (dry milling 30 h, wet milling 10 h).

The resulting high-entropy alloy powder ($Fe_{32.5}Co_{23.5}Ni_{25}Si_{15}Cu_{1}Nb_{3}$) is then mixed with a commercial 6 wt% binder. Subsequently, 0.8 g of the mixed HEA powder is weighed and poured into a T-core mold with an inner diameter of 7.5 mm and an outer diameter of 13.5 mm. The powder is compacted at 1,000 MPa, and the samples are annealed for 2 h at temperatures of 700 °C, 800 °C, and 900 °C. This toroidal sample is used for measurements of magnetic permeability, electrical resistivity, and porosity.

2.2. Materials characterization

The microstructure of the $Fe_{32.5}Co_{23.5}Ni_{25}Si_{15}Cu_{1}Nb_{3}$ HEA is observed using high-resolution scanning electron microscopy (HR-SEM, HITACHI SU8000), and the crystalline structure is examined by X-ray diffraction (XRD, Bruker D8 DISCOVER) with Cu-Kα ($\lambda = 0.15406$ nm) radiation. The diffraction angle (2θ) scanned from 20° to 90°. An investigation of the elemental composition was conducted, employing an X-ray energy dispersive spectrometer (EDS, Bruker XFlash 5060F) linked with HR-SEM.

The coercive force (H_c) and saturation magnetization (M_s) of the high-entropy alloy powder with different milling times are measured using a superconducting quantum interference device vibrating sample magnetometer (SQUID VSM, Quantum Design MPMS 3) under an applied magnetic field of 20,000 Oe. The complex magnetic permeability of the high-entropy alloy bulk material is measured using an impedance analyzer (Keysight E4990A) with a magnetic material test fixture (Keysight 16454A). The loss tangent is calculated by dividing the imaginary part of the magnetic permeability by the real part. The resistivity is calculated from the slope obtained from the current-voltage (J-E) curve measured using a source meter (Model 2410, Keithley). The pore distribution of the high-entropy alloy bulk material is measured using a surface area analyzer (ASAP 2020, Micromeritics). Based on the gas adsorption characteristics on the solid surface, the reversible physical adsorption of gas molecules on the surface of the bulk material at ultra-low temperatures corresponds to a specific adsorption amount at a certain pressure.

2.3. Simulation of wireless charging characteristics

The electromagnetic parameters of high-entropy alloys (HEAs) and traditional ferrites are simulated using the Ansys Maxwell software [71–74]. A 3D Maxwell module is created and imported to perform the simulation, which includes the analysis of magnetic fields, self-inductance, mutual inductance, and coupling coefficients, with the operating frequency set at 100 kHz. Subsequently, a simplified RLC circuit is created using the Ansys Simplorer software [75,76], and the 3D Maxwell module is imported to compare the efficiency differences between the magnetic shielding materials made from high-entropy alloys and commercial ferrites, specifically those using FeMnZn.

2.4. Fabrication of wireless charging devices

The $Fe_{32.5}Co_{23.5}Ni_{25}Si_{15}Cu_{1}Nb_{3}$ high-entropy alloy powder is used to create an electromagnetic shielding plate. It is uniformly mixed with a commercial 6 wt% binder, and 40 g of the mixed high-entropy alloy powder are weighed and poured into a T-core mold with an inner square of 60 mm × 60 mm and an outer diameter of 75 mm. The powder is compacted at 1,000 MPa pressure for 10 min per press, and this process is repeated twice. The sample is then placed in a quartz tube furnace for annealing at 800 °C for 2 h. The resulting HEA shielding plate is a square with dimensions of 60 mm × 60 mm × 1 mm.

Next, we used a 5W QI wireless charging transmitter module, model MTARD5V, produced by Lian Teng Electronic Co., Ltd. (Taiwan). The module specifications are a power input of DC 5V ± 0.25V and a current output of 1A. It includes a Printed Circuit Board Assembly (PCBA) (dimensions: 3.2 cm × 3.2 cm), a copper wire-wound coil (serving as the transmitter coil), and an Mn-Zn ferrite electromagnetic shielding plate as the base. We removed the original Mn-Zn ferrite electromagnetic shielding plate attached to the bottom of the transmitter coil and replaced it with the high-entropy alloy magnetic shielding plate fabricated in the previous section (as shown in the left image of Fig. 6(e)). This completed the mobile phone wireless charging device, with the high-entropy alloy serving as the magnetic shielding plate."

3. Results

Ball milling in mechanical alloying is the most crucial step in the powder processing. Dry milling provides higher collision energy, effectively reducing the powder volume, while wet milling helps produce smoother surfaces, enhancing powder flowability. This study employs a combination of dry and wet milling to optimize powder characteristics. Initially, dry milling is fixed at 5 h, and wet milling time is varied, designated as W0-W30, where the number represents the hours of wet milling. Fig. 1(a) shows the SEM morphology of the wet milling series (W-series). The particle size of the powder without wet milling (W0) is greater than 10 μm. After 5 h of milling (W5), flake structures begin to appear, and the size significantly decreases. W10 returns to a more rounded appearance. After 20 h of milling (W20), the size continues to decrease, but further milling up to 30 h (W30) results in only a slight reduction in particle size, indicating that the wet milling effect is nearing saturation.

For the dry milling series (D-series), the powder is fixed at 10 h of wet milling, while the dry milling time is varied, with samples designated as D0-D30. Note that D5 and W10 represent the same milling conditions. Fig. 1(b) shows the SEM morphology of D0-D30. It can be observed that after 0 h of dry milling and 10 h of wet milling, the powder has a round shape with particles larger than 20 μm. When the dry milling time increases to 13 h, the particle size is reduced to less than 20 μm, with the overall powder predominantly round. The results of 13 h of wet milling are almost identical to those of 15 h of wet milling. After 30 h of dry milling, it is evident that the particle size is significantly reduced to below 10 μm.

XRD was used to further analyze the phase composition of the W and D-series powders. The wet milling time (Fig. 2(a)) or the dry milling time (Fig. 2(d)) results in an increase in the full width at half maximum (FWHM) of the diffraction peaks and a shift of the peak positions to smaller angles, indicating changes in grain size, lattice strain, and crystallinity. Fig. 2(b–e) show the calculated results for grain size and lattice strain, while Fig. 2(c–f) present the changes in crystallinity with wet and dry milling times.

The average grain size is calculated using the Scherrer equation [77]:

$$D = \frac{k\lambda}{\beta \cos \theta} \tag{1}$$

where D is the average grain size (nm), λ is the X-ray wavelength (Cu Kα = 0.15406 nm), β is the peak FWHM, θ is the diffraction angle, and k = 0.9 is a constant.

The lattice strain is calculated using the Williamson-Hall method [78]:

$$\varepsilon = \frac{\beta}{4 \tan \theta} \tag{2}$$

where ε is the lattice strain, β is the peak width at half maximum, and θ is the diffraction angle. The crystallinity index (CI) is calculated using the method reported by Pardo et al. [79]:

$$CI = \frac{Ac}{A_c + A_a} \tag{3}$$

where A_c is the area under the crystalline peak, and A_a is the area under the amorphous peak. As the wet milling time increases, the grain size gradually decreases, lattice strain increases, and crystallinity reaches its highest value at 10 h of milling. During the dry milling process, the grain size first decreases and then increases, while the lattice strain first increases and then decreases, with the best crystallinity observed at 5 h.

Fig. 3 shows the magnetic properties of high-entropy powders produced under different milling conditions. In the W-series, as exhibited in

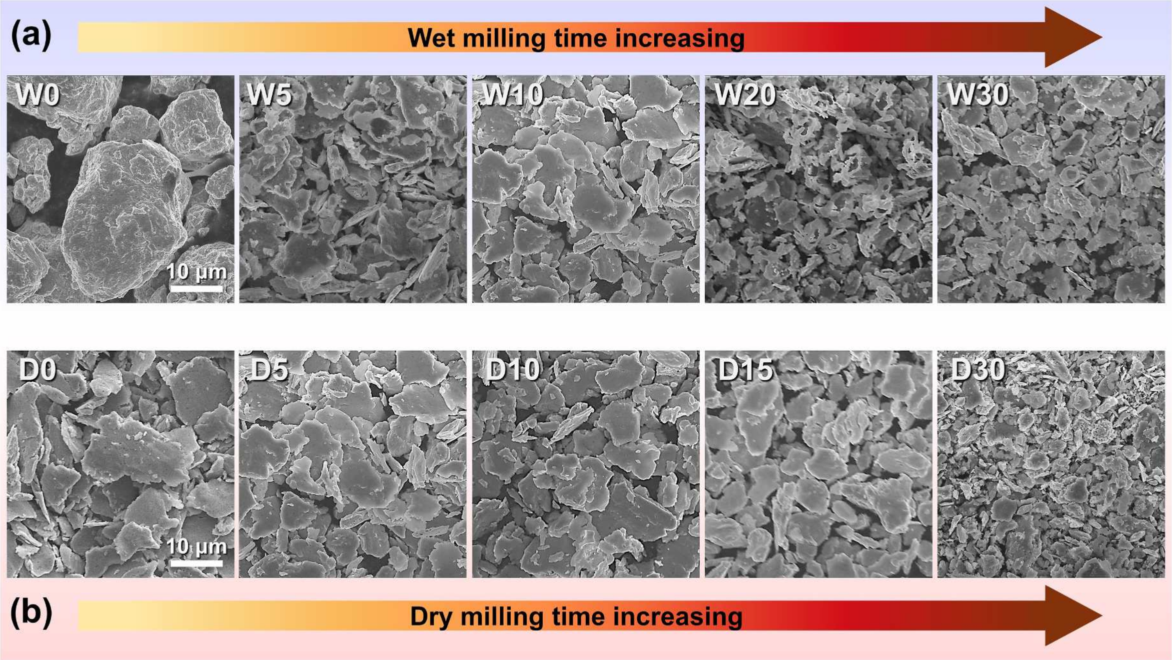

Fig. 1. SEM images of HEA powders with different dry milling and wet milling times. (a) D series: dry milling time fixed at 5 h, wet milling time varies from 0 to 30 h. (b) W series: wet milling time fixed at 10 h, dry milling time varies from 0 to 30 h. The mechanical alloying process sequence involves conducting dry milling first, followed by wet milling.

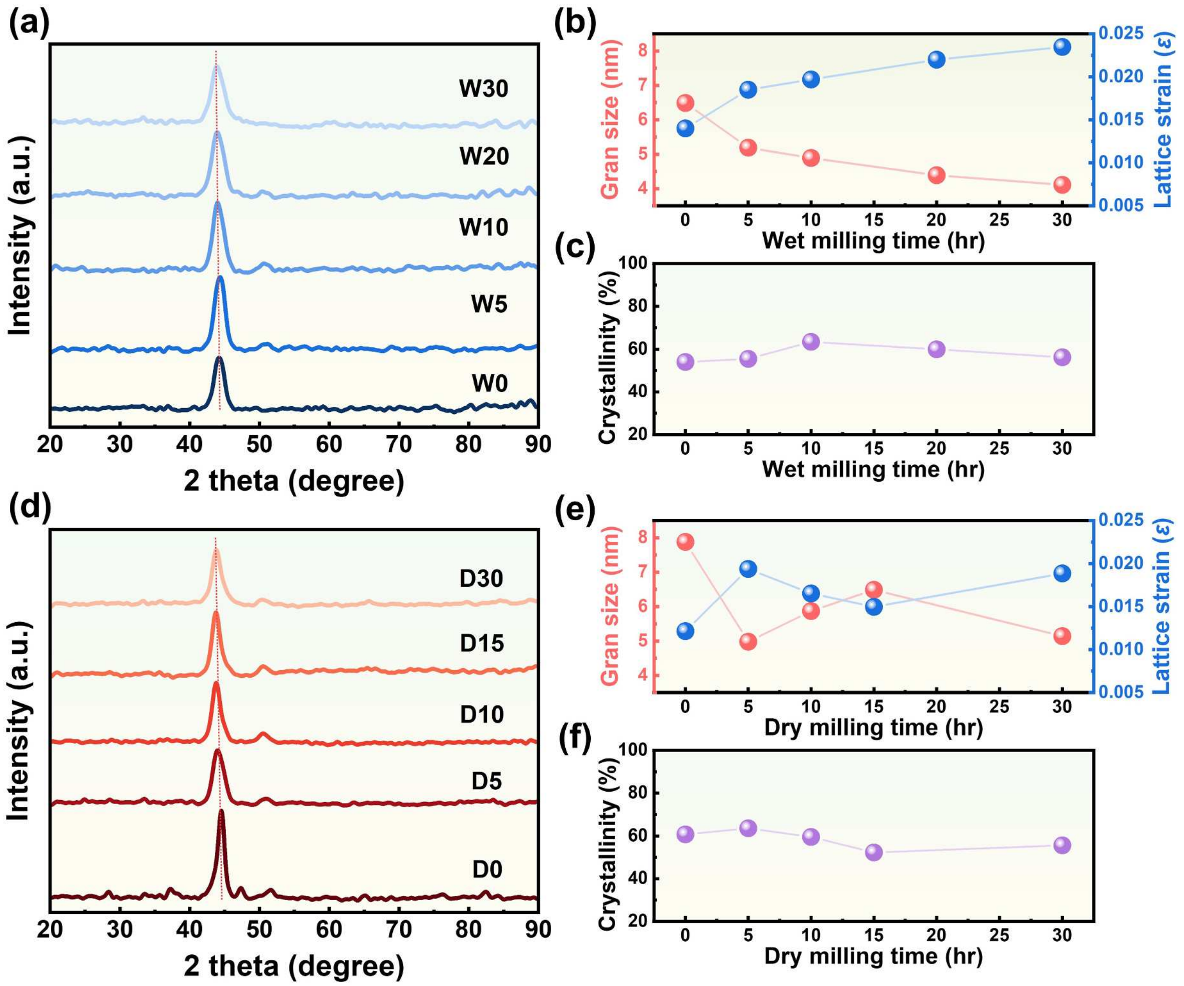

Fig. 2. (a) XRD patterns, (b) grain size and lattice strain, and (c) crystallinity of W series HEA powders. (d) XRD patterns, (e) grain size and lattice strain, and (f) crystallinity of D series HEA powders.

Fig. 3(a, b), W10 presents the highest saturation magnetization (M_s) and the lowest coercivity (H_c), making it most suitable for soft magnetic applications. This trend indicates that crystallinity primarily governs the magnetic properties of the dry milling series. In the D-Series, as shown in Fig. 3(c, d), D5 has the highest saturation magnetization, while the coercivity gradually decreases with increasing milling time. This result indicates that extending the dry milling time effectively reduces coercivity but also lowers the saturation magnetization. However, the M_s of D30 is 117.14 emu/g, which is slightly lower than that of D5. Nevertheless, the H_c of D30 decreases to 4.95, the lowest H_c observed in both the W and D-series. Considering the loss characteristics for subsequent wireless power transmission applications, we will still prioritize the D30 condition for further development of electromagnetic shielding materials. To further improve its saturation magnetization, we annealed the powder at temperatures ranging from 700 to 900 °C.

In Fig. 4(a), it is shown that as the annealing temperature increases, grain growth occurs and porosity gradually decreases. As presented in Fig. 4(b), the elemental mapping of Fe, Co, Ni, Si, Cu, and Nb indicates that the HEAs prepared by dry milling, followed by wet milling, and then annealed at 800 °C for 2 h, exhibit better elemental uniformity and stronger solid-solution ability. Fig. 4(c) shows that annealing transforms the powder from a single solid-solution phase achieved by ball milling to a mixed fcc and bcc phase. As shown in Fig. 4(d and e), calculations using the Scherrer formula reveal that grain size significantly increases upon annealing at 700 °C, with further temperature increases having little effect on grain size.

The magnetic hysteresis curves after annealing is presented in Fig. 5 (a), while Fig. 5(b) shows the effect of annealing temperature on M_s and H_c. It is evident that annealing at 700 °C yields the highest M_s and H_c values. Fig. 5(c) shows the effect of annealing temperature on porosity, with data indicating a significant decrease in porosity as the annealing temperature rises. As exhibited in Fig. 5(d), further measurements of resistivity changes reveal that annealing significantly reduces resistivity, explaining why the optimal M_s and H_c occur around 700 °C annealing despite the increase in grain size. Fig. 5(e and f) analyze the real and imaginary parts of the magnetic permeability of high-entropy alloys at different annealing temperatures. At an annealing temperature of 700 °C, the bulk material still has some small pores that adversely affect the formation and arrangement of magnetic domains. As the annealing temperature rises to 900 °C, the porosity in the material gradually decreases, and grain growth improves the integrity of the magnetic domains, the material's conductivity, and the real part of magnetic permeability. However, the decrease in resistivity due to high-temperature annealing leads to increased eddy current losses, resulting in higher imaginary magnetic permeability compared to other temperatures.

The tangent loss (tan δ) of the material can be described by the following formula:

$$\tan \delta = \frac{\mu''}{\mu'}, \tag{4}$$

where μ'' is the imaginary part of the magnetic permeability, and μ' is the

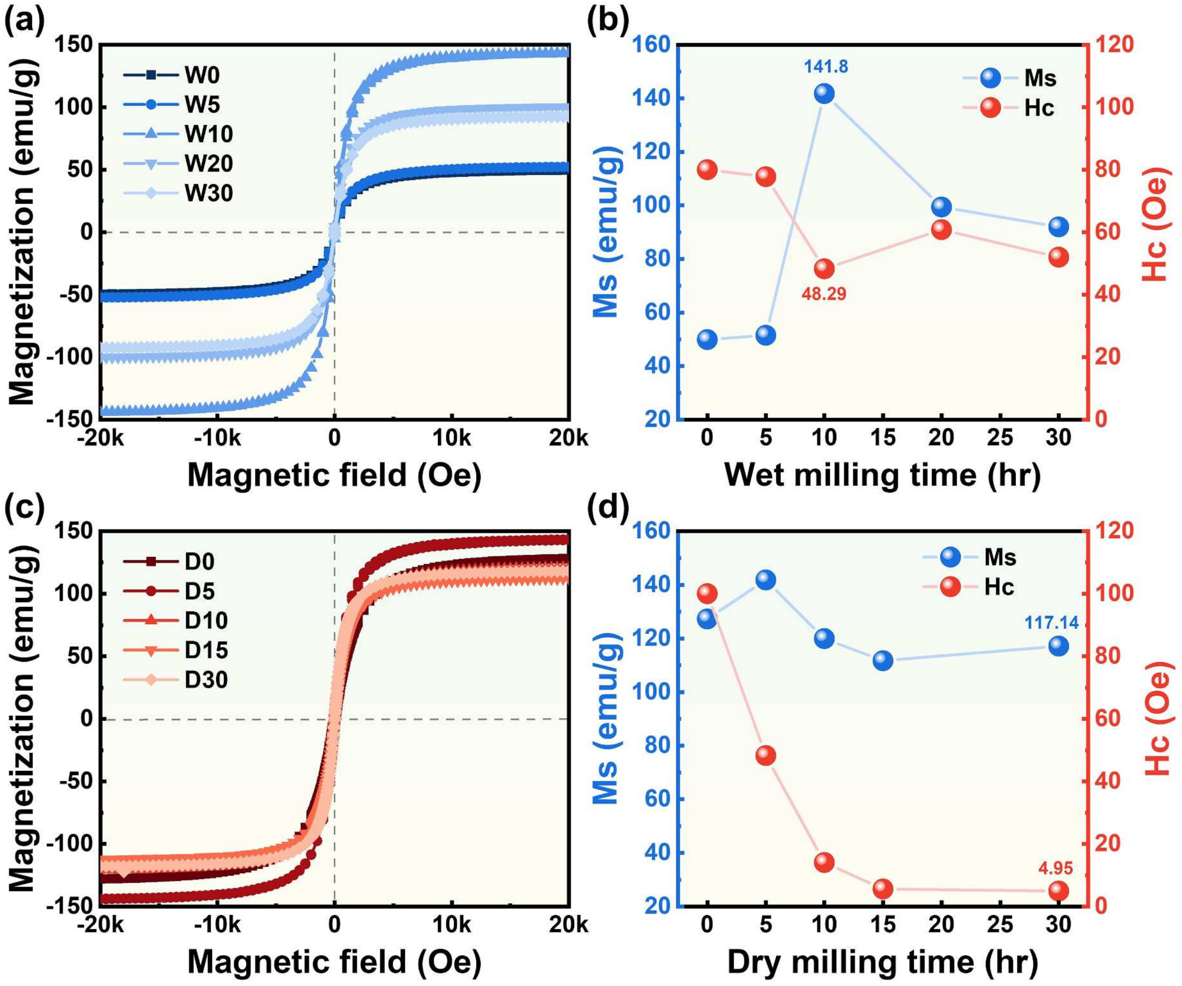

Fig. 3. Magnetic properties of the W series, showing (a) the hysteresis curve and (b) the saturation magnetization and coercive force. Magnetic properties of the D series, showing (c) the hysteresis curve and (d) the saturation magnetization and coercive force.

real part of the magnetic permeability.

The tangent loss of the material annealed at 800 °C is lower compared to the other two temperatures because the porosity at this temperature has significantly reduced, the resistivity has markedly decreased, and a better magnetic domain structure has formed. Table 1 summarizes the changes in the relevant material characteristics.

4. Discussion

Fig. 6 compares the soft magnetic properties of the D30 high-entropy alloy annealed at 800 °C (referred to as D30 800 °C) with a traditional soft magnetic material FeMnZn, which is sourced from the electromagnetic shielding materials of commonly available wireless charging modules for mobile phones. In Fig. 6(a), the hysteresis curves are presented, indicating that the saturation magnetization of HEAs is higher than that of traditional ferrites, though the coercivity is slightly higher as well. Fig. 6(b) plots M_s against temperature, revealing that at 600 K, the saturation magnetization of traditional ferrites is nearly 0 emu/g, whereas HEAs maintain a saturation magnetization of 22.8 emu/g at 1,000 K, indicating better suitability for high-temperature applications. For the D30 HEA annealed at 800 °C, during the M-T measurement heating process (at a heating rate of 3 °C per minute), a small amount of the fcc phase might still remain incompletely transformed, which causes a slight phase change when the temperature reaches around 750 K, resulting in a temporary kink in the M-T curve [66]. However, as shown in Fig. S1, during the cooling process, since the slight phase change of the fcc phase has already occurred during heating, no further phase transformation or structural change takes place during cooling, so no kink is observed. The complex permeability analysis of high-entropy alloys and traditional ferrites is displayed in Fig. 6(c and d), showing that at 100 KHz, the real part of the magnetic permeability of HEAs is greater than that of traditional ferrites. As exhibited in Fig. 6(e), the D30 800 °C HEA was fabricated into a 60 mm × 60 mm × 1 mm square plate. This plate was then applied as the magnetic shielding material for the transmitter coil in a commercially available mobile phone wireless charging module. The implementation successfully demonstrated the functionality and efficiency of wireless charging for mobile phones.

Compared to traditional binary alloy soft magnetic materials, such as Fe-Ni and Fe-Co alloys, which typically offer high permeability and saturation magnetization, they also suffer from increased eddy current losses due to higher electrical conductivity. The HEA maintains high permeability and saturation magnetization while benefiting from increased resistivity caused by lattice distortion. This results in lower magnetic losses than traditional ferrites, making HEA more promising for commercial applications. Table 2 analyzes the loss characteristics of HEAs and traditional ferrites, showing that the tangent loss of HEAs is lower, which is attributed to the higher resistivity of HEAs compared to traditional ferrites.

Next, we simulated the potential application of HEAs as magnetic shielding materials. The design diagram of the simulation is in Fig. S2, and the parameter table is in Table S1. Detailed simulation methods were described in **Supplementary Note 1**. As a result, Fig. 7(a–c) show

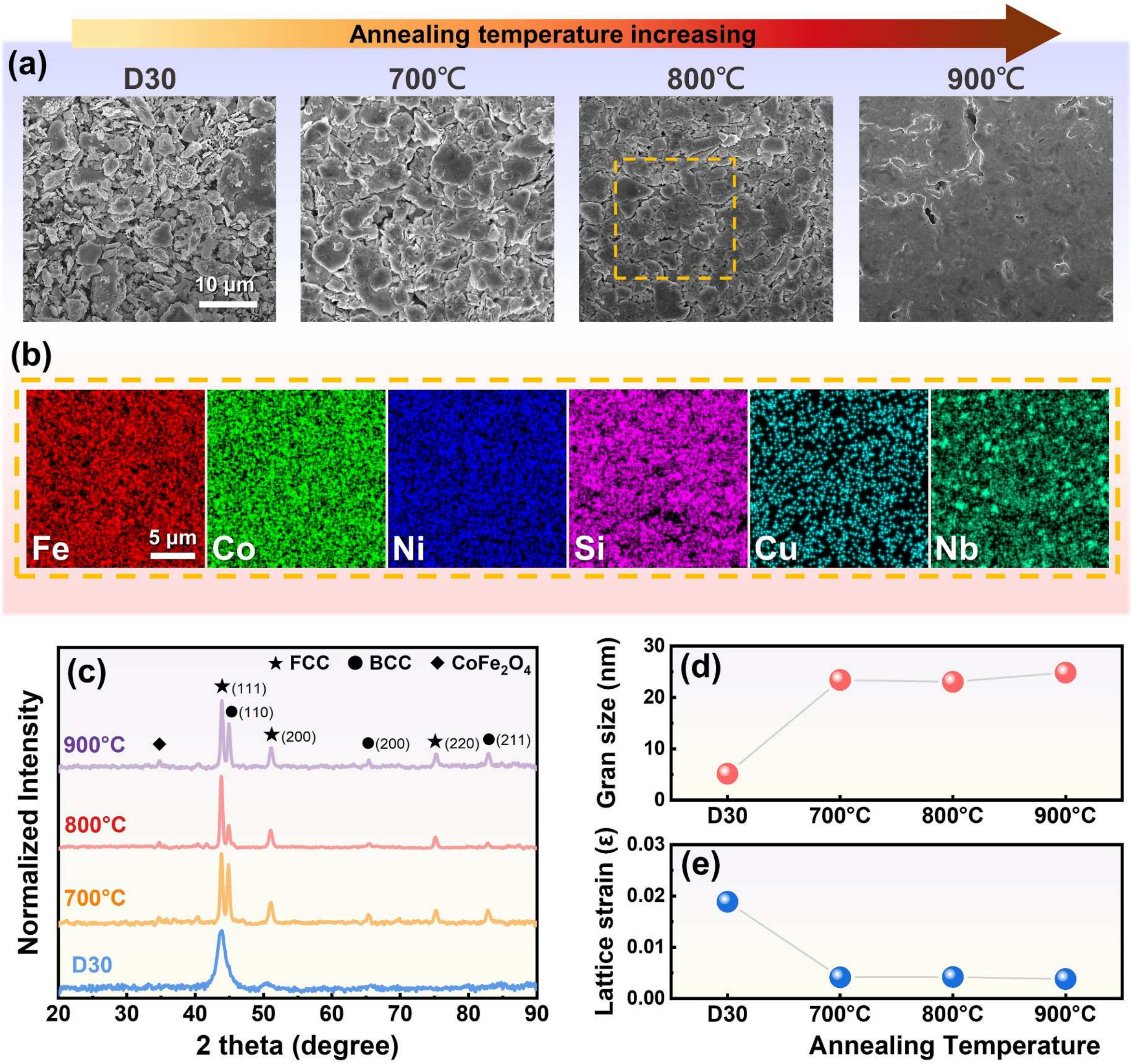

Fig. 4. (a) SEM images of D30 (dry milling 30 h, wet milling 10 h) HEA powder before annealing and after annealing at 700 °C, 800 °C, and 900 °C for 2 h. (b) EDS mapping of D30 HEA powder annealed at 800 °C. (c) Normalized XRD patterns, (d) grain size, and (e) lattice strain variations of the D30 HEA powder before and after annealing.

the magnetic field distribution in a wireless charging module. When the vertical distance is fixed at 10 mm and the horizontal distance is 0 mm, the magnetic field vector is transmitted from the transmitter to the receiver. Without adding magnetic shielding materials, the magnetic field vector exhibits significant divergence in Fig. 7(a), indicating lower energy transfer efficiency. Fig. 7(b and c) present the magnetic field distribution with traditional ferrites and HEAs as magnetic shielding materials, respectively. The HEA exhibits a more concentrated magnetic field vector, suggesting improved energy transfer efficiency, allowing the receiving coil to more effectively receive energy from the transmitting coil. Fig. 7(d) shows the calculated magnetic field strength comparison, where the HEA has a denser energy distribution, resulting in a larger magnetic field strength.

The coupling coefficient analysis of different magnetic shielding materials is presented in Fig. 7(e). In this analysis, we fixed the vertical distance (10 mm) and the horizontal distance (0 mm) to observe the impact of different magnetic shielding materials on the coupling coefficient. HEAs show better performance in terms of the coupling coefficient compared to traditional ferrites. This trend is due to the superior high resistivity and low loss tangent values of HEAs. These properties allow HEAs to more effectively confine the magnetic field, increasing the coupling coefficient and thereby improving the efficiency of energy transfer.

Fig. 7(f) presents the analysis results of self-inductance and mutual inductance under different magnetic shielding materials. In this analysis, we fixed the vertical distance (10 mm) and the horizontal distance (0 mm) to observe the impact of different magnetic shielding materials on self-inductance and mutual inductance. Without adding magnetic shielding materials, both self-inductance and mutual inductance are lower. This is because, in wireless charging, the coupling between the coils depends on the magnetic flux. When there is no magnetic shielding, the time-varying magnetic flux caused by the alternating current will partially dissipate into the surrounding environment, resulting in lower self-inductance and mutual inductance. When magnetic shielding materials are added, the magnetic flux is better confined, reducing magnetic field leakage and leading to higher self-inductance.

According to the formula for self-inductance:

$$L = N^2 \mu_r \mu_0 \left[ln\left(\frac{8r}{a}\right) - 2 + Y \right] \tag{5}$$

where N is the number of turns, μ_r is the relative permeability, r is the coil radius, a is the wire radius, and Y is a constant representing the

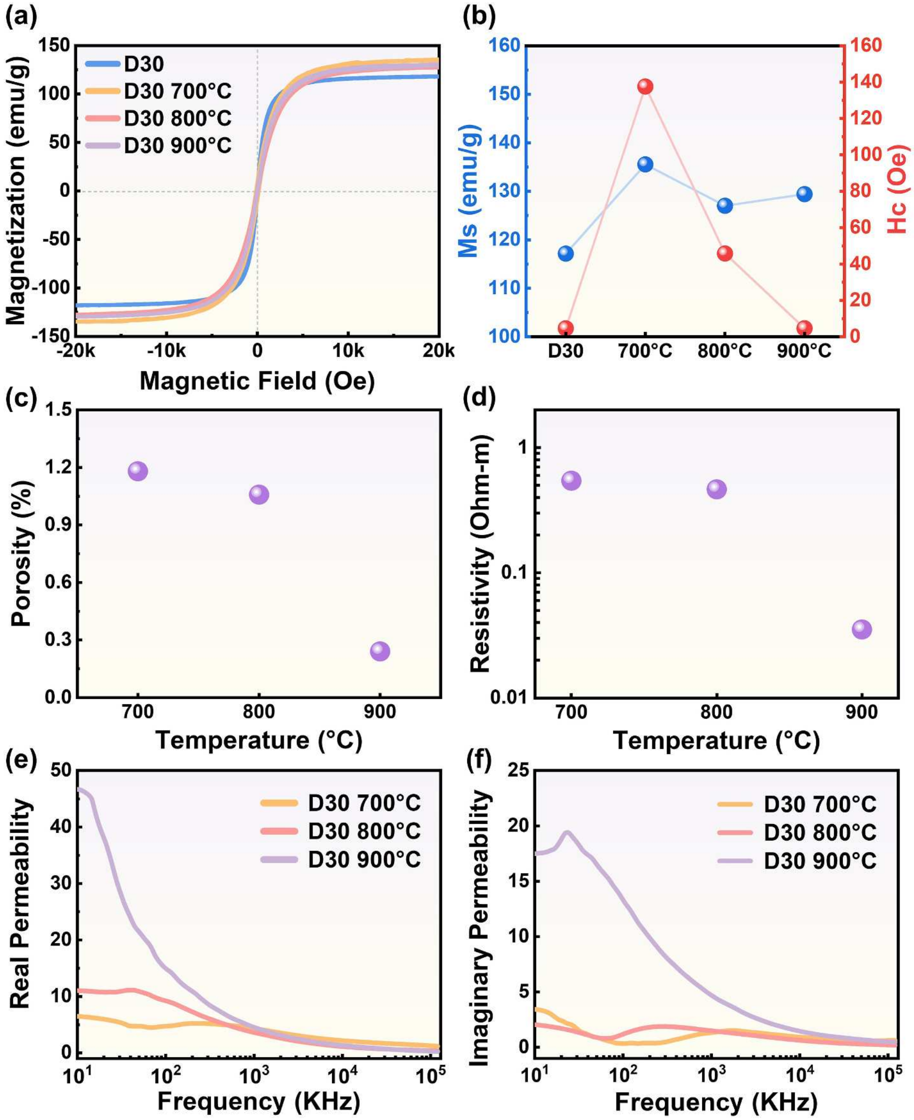

Fig. 5. Effects of annealing temperature on the D30 HEA powder, including (a) hysteresis curve and (b) saturation magnetization and coercive force. Measurements of D30 toroidal samples include (c) porosity, (d) resistivity, (e) real part of permittivity, and (f) imaginary part of permittivity.

current distribution.

When $Y = 0$, it indicates that the current flows uniformly on the surface of the wire, whereas $Y = 0.25$ suggests that the current is uniformly distributed within the wire [80]. Thus, the value of self-inductance is proportional to the permeability. Lower permeability results in lower self-inductance values. In contrast, HEAs, with their higher permeability, exhibit higher self-inductance values.

The efficiency analysis of traditional ferrites and HEAs is shown in Fig. 7(g), where AC-AC efficiency is the ratio of the output to input power [81]. The results show that the efficiency of HEAs is 19 % higher than that of traditional ferrites. The lower power transmission efficiency of traditional ferrites compared to HEAs could be due to the following reasons. First, the difference in Coupling Coefficient: The coupling coefficient plays an important role in wireless charging circuits. It indicates that the degree of magnetic coupling between the transmitting and receiving coils directly affects the power transmission efficiency. The higher permeability of HEAs leads to a higher mutual inductance to inductance ratio, resulting in a higher coupling coefficient. Therefore, at the same input power, HEA circuits can achieve higher power transmission efficiency. Second, difference in Eddy current loss: Besides the coupling coefficient, eddy current loss is another critical factor affecting the power transmission efficiency. The eddy current loss is the energy loss caused by induced currents within the material due to the magnetic field. HEAs have higher resistivity, thus generating lower eddy current losses when the current passes through them, compared to traditional ferrites. This advantage makes HEA circuits experience lower eddy current losses, thereby enhancing power transmission efficiency.

5. Conclusion

The present research develops HEA soft magnetic materials for low-frequency magnetic shielding applications. The $Fe_{32.5}Co_{23.5}Ni_{25}Si_{15}$-$Cu_1Nb_3$ HEA, synthesized through dry milling, followed by wet milling and annealing at 800 °C, exhibits superior soft magnetic properties, better element uniformity, and stronger solid solution ability. Compared to the traditional electromagnetic shielding material FeMnZn, HEAs demonstrate exceptional high-temperature stability, retaining a saturation magnetization of 22.8 emu/g at 1,000K, whereas the FeMnZn drops to nearly 0 emu/g at 600K. Additionally, the higher magnetic permeability of HEAs results in a higher mutual inductance to inductance ratio, achieving a coupling coefficient of up to 0.84. The lower loss tangent of HEAs reduces eddy current losses, enhancing the wireless power transmission efficiency by 19 %.

Furthermore, the practical application of this HEA material in the

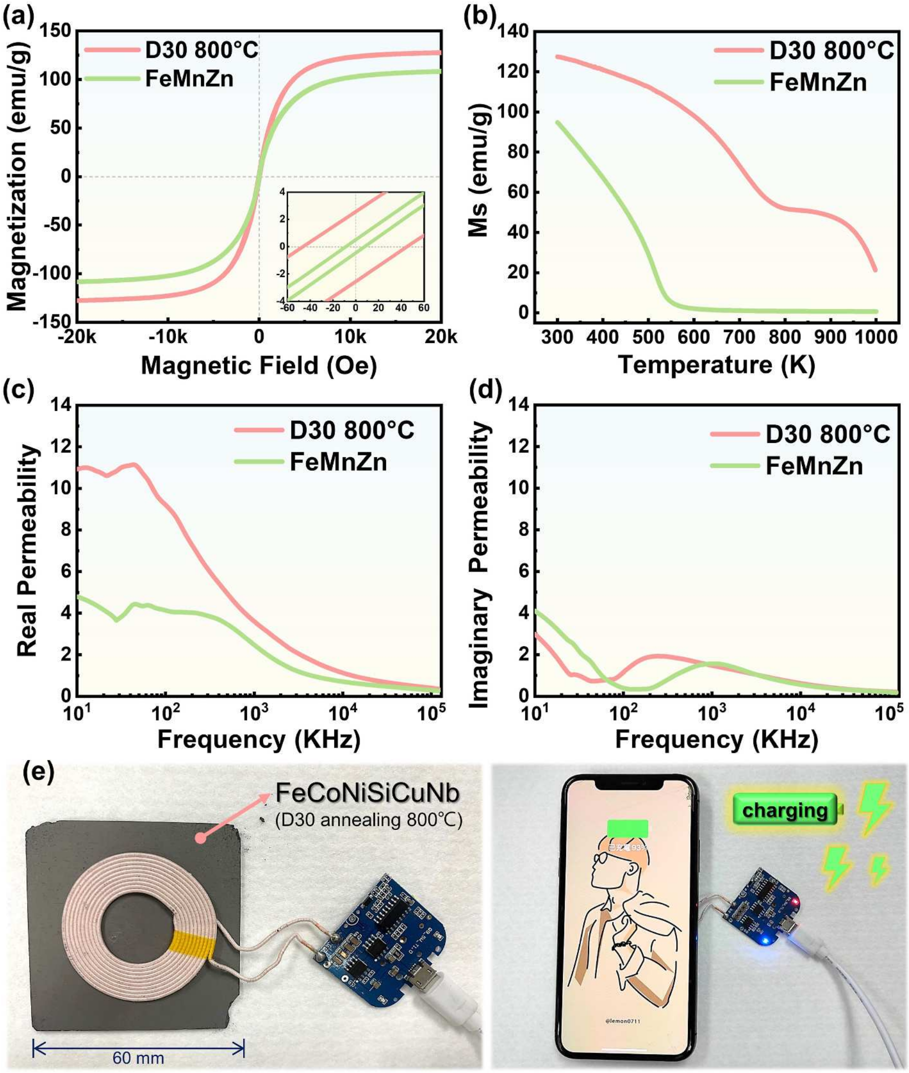

Fig. 6. Comparative analysis of the magnetic properties of the D30 HEA powder annealed at 800 °C and the commercial electromagnetic shielding material $Fe_{70}Mn_{20}Zn_{10}$, including (a) hysteresis curves, (b) Curie temperature characteristics measured from 300K to 1,000K, (c) real part of permittivity, and (d) imaginary part of permittivity. (e) Demonstration of a wireless charging module using an electromagnetic shielding plate made from the HEA with dimensions of 60 mm × 60 mm × 1 mm, positioned above the transmitter coil, successfully displaying the functionality of wireless charging for a mobile phone.

Table 1
Electromagnetic properties, porosity, and resistivity measurements of the D30 high-entropy alloy at different annealing temperatures.

D30 Annealing Temp.	Dielectric Loss Tangent (f = 100 KHz)	M_s (emu/g)	H_c (Oe)	Porosity (%)	Resistivity (Ω-m)
700 °C	0.06	137.53	137.55	1.18	0.54
800 °C	0.05	126.3	44.4	1.05	0.46
900 °C	0.89	129.41	4.65	0.24	0.03

Table 2
Electromagnetic properties and resistivity measurements of the D30 high-entropy alloy (annealed at 800 °C) compared to the commercial magnetic shielding material FeMnZn.

Materials	Dielectric Loss Tangent (f = 100 KHz)	M_s (emu/g)	H_c (Oe)	Resistivity (Ω-m)
D30 annealing 800 °C	0.05	126.3	44.4	0.46
FeMnZn	0.13	105.8	10.8	0.21

electromagnetic shielding plate of the transmitter coil in commercial wireless charging modules for mobile phones successfully demonstrated the functionality of wireless charging. These findings highlight the potential of HEAs in improving the performance and efficiency of wireless power transmission systems, making them a promising material for future technological advancements in this field.

CRediT authorship contribution statement

Cheng-Hsien Yeh: Writing – original draft, Visualization, Validation, Formal analysis. **Chia-Hua Hu:** Writing – original draft, Methodology, Investigation. **Hsuan-Ta Wu:** Supervision, Methodology. **Wen-Dung Hsu:** Supervision, Software, Conceptualization. **Bernard Hao-chih Liu:** Visualization, Supervision, Resources. **Peter K. Liaw:** Writing – review & editing, Funding acquisition. **Chuan-Feng Shih:** Writing – review & editing, Supervision, Funding acquisition, Conceptualization.

Declaration of competing interest

The author is an Editorial Board Member/Editor-in-Chief/Associate Editor/Guest Editor for *Materials Today Advances* and was not involved

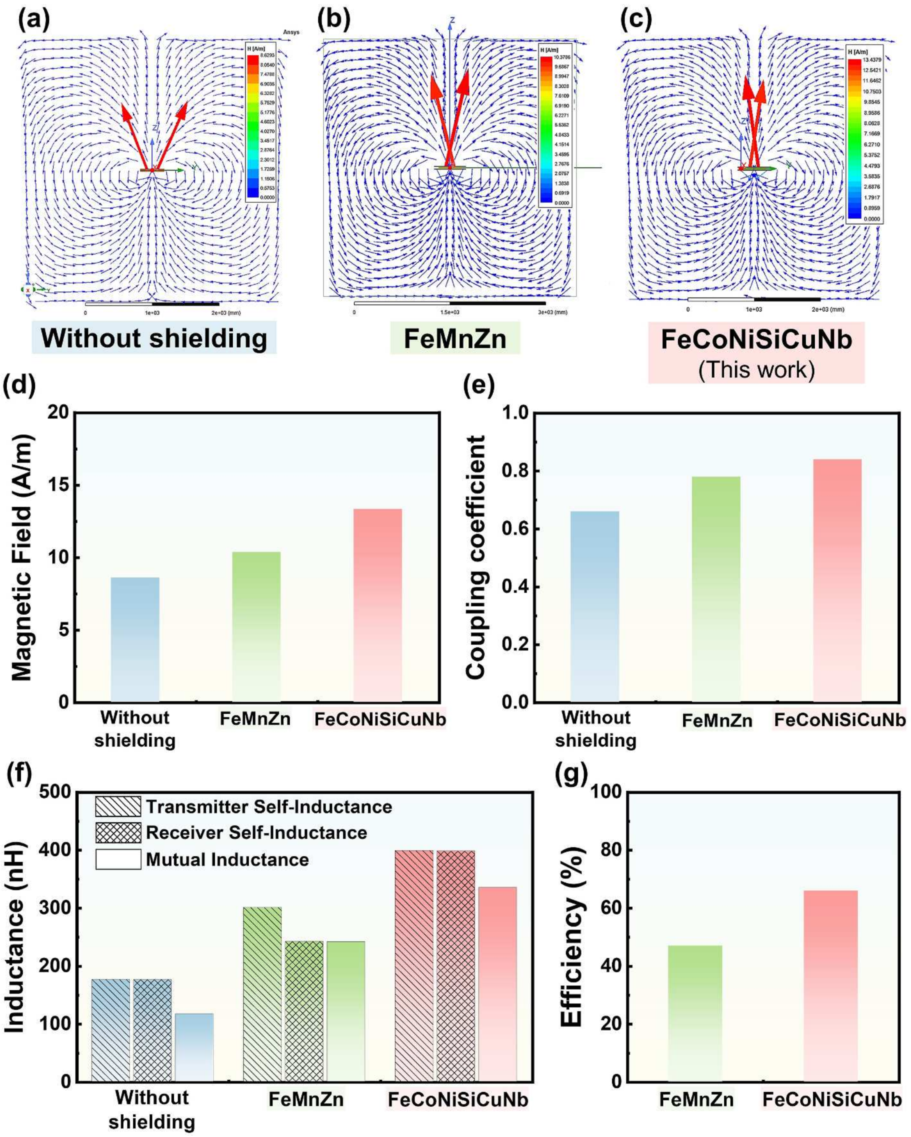

Fig. 7. Three-dimensional electromagnetic field simulation and analysis of wireless charging (f = 100 kHz) using the Ansys Maxwell software. The overall magnetic field strength analysis includes (a) no electromagnetic shielding material, (b) FeMnZn material, and (c) FeCoNiSiCuNb high-entropy alloy. Additionally, (d) magnetic field intensity, (e) coupling coefficient, (f) inductance characteristics, including self-inductance and mutual inductance analysis, and (g) wireless transmission efficiency.

in the editorial review or the decision to publish this article.

The authors declare the following financial interests/personal relationships which may be considered as potential competing interests: Chuan-Feng Shih reports financial support was provided by National Science and Technology Council, R.O.C. Chuan-Feng Shih reports financial support was provided by Taiwan Semiconductor Research Institute. Peter K. Liaw reports financial support was provided by National Science Foundation, USA. Peter K. Liaw reports financial support was provided by Army Research Office, USA. If there are other authors, they declare that they have no known competing financial interests or personal relationships that could have appeared to influence the work reported in this paper.

Acknowledgements

This work was financially supported by the National Science and Technology Council in Taiwan [grant numbers NSTC 113-2224-E-006-001 and 113-2221-E-006-078]; the Taiwan Semiconductor Research Institute [grant number JDP113-Y1-028]; the National Science Foundation [grant numbers DMR-1611180, 1809640, and 2226508]; and the Army Research Office [grant numbers W911NF-13-1-0438, W911NF-19-2-0049, and FA9550-23-1-0503]. The present research was supported in part by Higher Education Sprout Project at National Cheng Kung University (NCKU), Ministry of Education to the Headquarters of University Advancement at National Cheng Kung University (NCKU). Financial support of Applied High Entropy Technology (AHET) Center at National Cheng Kung University (NCKU), and Hierarchical Green-Energy Materials (Hi-GEM) Research Center, from The Featured Areas Research Center Program within the framework of the Higher Education Sprout Project by the Ministry of Education (MOE) in Taiwan.

The authors appreciate the support from the authors appreciate the technical support of the Core Facility Center of National Cheng Kung University for the use of HR-SEM (Hitachi SU8000), EDS (Bruker XFlash 5060 F), and SQUID VSM (Quantum Design MPMS 3).

Appendix A. Supplementary data

Supplementary data to this article can be found online at https://doi.

org/10.1016/j.mtadv.2024.100540.

Data availability

Data will be made available on request.

References

[1] X. Liu, Y. Duan, Y. Guo, H. Pang, Z. Li, X. Sun, T. Wang, Microstructure design of high-entropy alloys through a multistage mechanical alloying strategy for temperature-stable megahertz electromagnetic absorption, Nano-Micro Lett. 14 (1) (2022) 142.

[2] M. Ma, X. Zhao, X. Sun, J. Jiang, W. Shao, L. Zhen, Microstructure evolution and strengthening mechanism of FeCo-1.5V0.5Nb0.4 W soft magnetic alloy rolled strip with high yield strength and low coercivity, Acta Mater. 268 (2024) 119793.

[3] J. Yang, X. Zhang, M. Shi, S. Yuan, L. Wang, B. Han, Modeling and application of magnetic shaking for improving permeability and performance of magnetic shields, IEEE Trans. Ind. Electron. 71 (7) (2024) 8165–8175.

[4] Y. Ma, Q. Wang, X. Zhou, J. Hao, B. Gault, Q. Zhang, C. Dong, T.G. Nieh, A novel soft-magnetic B2-based multiprincipal-element alloy with a uniform distribution of coherent body-centered-cubic nanoprecipitates, Adv. Mater. 33 (14) (2021) 2006723.

[5] M. Liu, Z. Wang, Z. Song, F. Wang, G. Zhao, H. Zhu, Z. Jia, Z. Guo, F. Kang, C. Yang, A popcorn-inspired strategy for compounding graphene@NiFe2O4 flexible films for strong electromagnetic interference shielding and absorption, Nat. Commun. 15 (1) (2024) 5486.

[6] X. Liu, Y. Duan, Z. Li, H. Pang, L. Huang, X. Yang, Y. Shi, T. Wang, X. Lv, FeCoNiCr0.4CuX high-entropy alloys with strong intergranular magnetic coupling for stable megahertz electromagnetic absorption in a wide temperature spectrum, ACS Appl. Mater. Interfaces 14 (5) (2022) 7012–7021.

[7] K. Lakshmi, H. John, K.T. Mathew, R. Joseph, K.E. George, Microwave absorption, reflection and EMI shielding of PU–PANI composite, Acta Mater. 57 (2) (2009) 371–375.

[8] K. Tian, D. Hu, Q. Wei, Q. Fu, H. Deng, Recent progress on multifunctional electromagnetic interference shielding polymer composites, J. Mater. Sci. Technol. 134 (2023) 106–131.

[9] Z. Zhang, T. Gao, R. Zhao, C. Hu, Y. Liao, X. Liu, Z. Zhang, Y. Li, X. Zhang, High easy-plane anisotropy Y-Co intermetallic nanoparticles for boosting gigahertz magnetic loss ability, Acta Mater. 272 (2024) 119947.

[10] S.Y. Lee, Y.S. Lim, I.H. Choi, D.I. Lee, S.B. Kim, Effective combination of soft magnetic materials for magnetic shielding, IEEE Trans. Magn. 48 (11) (2012) 4550–4553.

[11] G. Ouyang, X. Chen, Y. Liang, C. Macziewski, J. Cui, Review of Fe-6.5 wt%Si high silicon steel—a promising soft magnetic material for sub-kHz application, J. Magn. Magn Mater. 481 (2019) 234–250.

[12] C. Meng, M. Liu, T. Li, Q. Man, D. Xue, New soft magnetic materials (Y1−xSmx) 2Fe14B with tunable magnetic anisotropy, Acta Mater. 276 (2024) 120090.

[13] K. Tashiro, I. Sasada, A low-cost magnetic shield consisting of nonoriented silicon steel, IEEE Trans. Magn. 41 (10) (2005) 4081–4083.

[14] X. Liu, Z. Yu, R. Ishikawa, L. Chen, X. Liu, X. Yin, Y. Ikuhara, R. Riedel, Single-source-precursor derived RGO/CNTs-SiCN ceramic nanocomposite with ultra-high electromagnetic shielding effectiveness, Acta Mater. 130 (2017) 83–93.

[15] H. Lee, S.H. Ryu, S.J. Kwon, J.R. Choi, S.-b. Lee, B. Park, Absorption-dominant mmWave EMI shielding films with ultralow reflection using ferromagnetic resonance frequency tunable M-type ferrites, Nano-Micro Lett. 15 (1) (2023) 76.

[16] Y. Wang, L. Yao, Q. Zheng, M.-S. Cao, Graphene-wrapped multiloculated nickel ferrite: a highly efficient electromagnetic attenuation material for microwave absorbing and green shielding, Nano Res. 15 (7) (2022) 6751–6760.

[17] H. Pang, Y. Duan, M. Gao, L. Huang, X. Liu, Z. Li, Electromagnetic wave absorption performance of FeCoNiMn0.5Al0.2 high entropy alloys governed by nanocrystal evolution, Materials Today Nano 20 (2022) 100243.

[18] P. Wu, J. Cui, K. Wang, Y. Huang, L. Qiao, T. Wang, F. Li, Study on the influence of the degree of the easy-plane orientation on the high-frequency magnetic properties and power loss of SMC in the MHz band, Acta Mater. 275 (2024) 120041.

[19] H. Pang, Y. Duan, X. Dai, L. Huang, X. Yang, T. Zhang, X. Liu, The electromagnetic response of composition-regulated honeycomb structural materials used for broadband microwave absorption, J. Mater. Sci. Technol. 88 (2021) 203–214.

[20] W. Li, H. Cai, Y. Kang, Y. Ying, J. Yu, J. Zheng, L. Qiao, Y. Jiang, S. Che, High permeability and low loss bioinspired soft magnetic composites with nacre-like structure for high frequency applications, Acta Mater. 167 (2019) 267–274.

[21] Z. Li, K.G. Pradeep, Y. Deng, D. Raabe, C.C. Tasan, Metastable high-entropy dual-phase alloys overcome the strength–ductility trade-off, Nature 534 (7606) (2016) 227–230.

[22] Z. Lei, X. Liu, Y. Wu, H. Wang, S. Jiang, S. Wang, X. Hui, Y. Wu, B. Gault, P. Kontis, D. Raabe, L. Gu, Q. Zhang, H. Chen, H. Wang, J. Liu, K. An, Q. Zeng, T.-G. Nieh, Z. Lu, Enhanced strength and ductility in a high-entropy alloy via ordered oxygen complexes, Nature 563 (7732) (2018) 546–550.

[23] Q. Pan, L. Zhang, R. Feng, Q. Lu, K. An, A.C. Chuang, J.D. Poplawsky, P.K. Liaw, L. Lu, Gradient cell–structured high-entropy alloy with exceptional strength and ductility, Science 374 (6570) (2021) 984–989.

[24] Z. Li, Z. Zhang, X. Liu, H. Li, E. Zhang, G. Bai, H. Xu, X. Liu, X. Zhang, Strength, plasticity and coercivity tradeoff in soft magnetic high-entropy alloys by multiple coherent interfaces, Acta Mater. 254 (2023) 118970.

[25] C. Lee, F. Maresca, R. Feng, Y. Chou, T. Ungar, M. Widom, K. An, J.D. Poplawsky, Y.-C. Chou, P.K. Liaw, W.A. Curtin, Strength can be controlled by edge dislocations in refractory high-entropy alloys, Nat. Commun. 12 (1) (2021) 5474.

[26] T. Tsuru, S. Han, S. Matsuura, Z. Chen, K. Kishida, I. Iobzenko, S.I. Rao, C. Woodward, E.P. George, H. Inui, Intrinsic factors responsible for brittle versus ductile nature of refractory high-entropy alloys, Nat. Commun. 15 (1) (2024) 1706.

[27] C. Niu, C.R. LaRosa, J. Miao, M.J. Mills, M. Ghazisaeidi, Magnetically-driven phase transformation strengthening in high entropy alloys, Nat. Commun. 9 (1) (2018) 1363.

[28] A. Kovács, N.B. Venkataraman, V. Chaudhary, S. Dasari, T. Denneulin, R. V. Ramanujan, R. Banerjee, R.E. Dunin-Borkowski, Role of heterophase interfaces on local coercivity mechanisms in the magnetic Al0.3CoFeNi complex concentrated alloy, Acta Mater. 246 (2023) 118672.

[29] C. Jung, K. Kang, A. Marshal, K.G. Pradeep, J.-B. Seol, H.M. Lee, P.-P. Choi, Effects of phase composition and elemental partitioning on soft magnetic properties of AlFeCoCrMn high entropy alloys, Acta Mater. 171 (2019) 31–39.

[30] C.-H. Yeh, W.-D. Hsu, B.H. Liu, C.-S. Yang, C.-Y. Kuan, Y.-C. Chang, K.-S. Huang, S.-S. Jhang, C.-Y. Lu, P.K. Liaw, C.-F. Shih, Low-frequency conductivity of low wear high-entropy alloys, Nat. Commun. 15 (1) (2024) 4554.

[31] C.-H. Yeh, H.-S. You, Y.-C. Chang, C.-Y. Kuan, H.-T. Wu, W.-D. Hsu, C.-F. Shih, Design of high-entropy films as ultra-violet light reflector, Appl. Mater. Today 36 (2024) 102013.

[32] J.W. Yeh, S.K. Chen, S.J. Lin, J.Y. Gan, T.S. Chin, T.T. Shun, C.H. Tsau, S.Y. Chang, Nanostructured high-entropy alloys with multiple principal elements: novel alloy design concepts and outcomes, Adv. Eng. Mater. 6 (5) (2004) 299–303.

[33] B. Cantor, I.T.H. Chang, P. Knight, A.J.B. Vincent, Microstructural development in equiatomic multicomponent alloys, Mater. Sci. Eng., A 375–377 (2004) 213–218.

[34] B. Yang, J. Fang, C. Xu, H. Cao, R. Zhang, B. Zhao, M. Huang, X. Wang, H. Lv, R. Che, One-dimensional magnetic FeCoNi alloy toward low-frequency electromagnetic wave absorption, Nano-Micro Lett. 14 (1) (2022) 170.

[35] Z. Yingzhe, C. Yudao, Q. Qingdong, L. Wei, Synthesis of FeCoNiCuZn single-phase high-entropy alloy by high-frequency electromagnetic-field assisted ball milling, J. Magn. Magn Mater. 498 (2020) 166151.

[36] J. He, H. Wang, H. Huang, X. Xu, M. Chen, Y. Wu, X. Liu, T. Nieh, K. An, Z. Lu, A precipitation-hardened high-entropy alloy with outstanding tensile properties, Acta Mater. 102 (2016) 187–196.

[37] Y. Brif, M. Thomas, I. Todd, The use of high-entropy alloys in additive manufacturing, Scripta Mater. 99 (2015) 93–96.

[38] J. Menghani, A. Vyas, P. Patel, H. Natu, S. More, Wear, erosion and corrosion behavior of laser cladded high entropy alloy coatings–A review, Mater. Today: Proc. 38 (2021) 2824–2829.

[39] A.Y. Churyumov, A. Pozdniakov, A. Bazlov, H. Mao, V. Polkin, D. Louzguine-Luzgin, Effect of Nb addition on microstructure and thermal and mechanical properties of Fe-Co-Ni-Cu-Cr multiprincipal-element (high-entropy) alloys in as-cast and heat-treated state, Jom 71 (10) (2019) 3481–3489.

[40] H. Zhang, Y. Pan, Y.-Z. He, Synthesis and characterization of FeCoNiCrCu high-entropy alloy coating by laser cladding, Mater. Des. 32 (4) (2011) 1910–1915.

[41] Y.-J. Hsu, W.-C. Chiang, J.-K. Wu, Corrosion behavior of FeCoNiCrCux high-entropy alloys in 3.5% sodium chloride solution, Mater. Chem. Phys. 92 (1) (2005) 112–117.

[42] L. Jia, L. Jiang, W. Zheng, J. Wu, J. Feng, Function of Si on the high-temperature oxidation of FeCoNiMnSix HEAs with excellent electromagnetic-wave absorption properties, J. Alloys Compd. 950 (2023) 169853.

[43] V. Chaudhary, R. Chaudhary, R. Banerjee, R.V. Ramanujan, Accelerated and conventional development of magnetic high entropy alloys, Mater. Today 49 (2021) 231–252.

[44] S. Dasari, V. Chaudhary, B. Gwalani, A. Jagetia, V. Soni, S. Gorsse, R. V. Ramanujan, R. Banerjee, Highly tunable magnetic and mechanical properties in an Al0.3CoFeNi complex concentrated alloy, Materialia 12 (2020).

[45] Y. Duan, X. Wen, B. Zhang, G. Ma, T. Wang, Optimizing the electromagnetic properties of the FeCoNiAlCrx high entropy alloy powders by composition adjustment and annealing treatment, J. Magn. Magn Mater. 497 (2020) 165947.

[46] X.J. Liu, Y.P. Duan, Y. Guo, H.F. Pang, Z.R. Li, X.Y. Sun, T.M. Wang, Microstructure design of high-entropy alloys through a multistage mechanical alloying strategy for temperature-stable megahertz electromagnetic absorption, Nano-Micro Lett. 14 (1) (2022).

[47] P. Yang, Y. Liu, X. Zhao, J. Cheng, H. Li, Electromagnetic wave absorption properties of mechanically alloyed FeCoNiCrAl high entropy alloy powders, Adv. Powder Technol. 27 (4) (2016) 1128–1133.

[48] Y. Zhang, B. Zhang, K. Li, G.-L. Zhao, S.M. Guo, Electromagnetic interference shielding effectiveness of high entropy AlCoCrFeNi alloy powder laden composites, J. Alloys Compd. 734 (2018) 220–228.

[49] B. Zhang, Y. Duan, X. Wen, G. Ma, T. Wang, X. Dong, H. Zhang, N. Jia, Y. Zeng, FeCoNiSixAl0.4 high entropy alloy powders with dual-phase microstructure: improving microwave absorbing properties via controlling phase transition, J. Alloys Compd. 790 (2019) 179–188.

[50] J. Calvo-de la Rosa, J. Tejada, A. Lousa, Structural and impedance spectroscopy characterization of soft magnetic materials, J. Magn. Magn Mater. 475 (2019) 570–578.

[51] A.D. Goodall, L. Chechik, F. Livera, I. Todd, Importance of surface roughness on the magnetic properties of additively manufactured FeSi thin walls, Acta Mater. 263 (2024) 119501.

[52] J. He, H. Yuan, M. Nie, H. Guo, H. Yu, Z. Liu, R. Sun, Soft magnetic materials for power inductors: state of art and future development, Materials Today Electronics 6 (2023) 100066.

[53] W. Li, W. Xiang, Y. Kang, T. Zou, X. Han, Y. Ying, J. Yu, J. Zheng, L. Qiao, J. Li, S. Che, Soft magnetism enhancement and eddy current suppression in bioinspired Iron-based nanocrystalline soft magnetic composites with nacre-like structure, J. Mater. Sci. Technol. 206 (2025) 202–210. https://doi.org/10.1016/j.jmst.2024.04.002.
[54] M. Yang, Q. Yang, Y. Li, Z. Lin, S. Yue, H. Wang, A.S. Bahman, Application-Oriented characterization and analysis of core materials under medium-frequency condition, IEEE Trans. Power Electron. 38 (9) (2023) 11245–11259.
[55] Y. Wang, C.Q. Jiang, L. Mo, J. Xiang, Z. Luo, W. Miao, Magnetic analysis of permeability configurable nanocrystalline flake ribbons for medium frequency energy conversion applications, Materials Today Sustainability 27 (2024) 100795.
[56] A.M. Leary, P.R. Ohodnicki, M.E. McHenry, Soft magnetic materials in high-frequency, high-power conversion applications, JOM 64 (7) (2012) 772–781.
[57] C. Jiang, X. Li, S.S. Ghosh, H. Zhao, Y. Shen, T. Long, Nanocrystalline powder cores for high-power high-frequency power electronics applications, IEEE Trans. Power Electron. 35 (10) (2020) 10821–10830.
[58] U. Adriano, O. Bottauscio, M. Zucca, Material efficiency in magnetic shielding at low and intermediate frequency, IEEE Trans. Magn. 39 (5) (2003) 3217–3219.
[59] X. Zhang, X. Ni, B. Wei, S. Wang, Q. Yang, Characteristic analysis of electromagnetic force in a high-power wireless power transfer system, Energies 11 (11) (2018) 3088.
[60] M. Zhou, X. Zhang, Regulating the recrystallized grain to induce strong cube texture in oriented silicon steel, J. Mater. Sci. Technol. 96 (2022) 126–139.
[61] Q. Zhang, S. Wang, J. Qiu, X. Jing, C. Gao, J.G. Zhu, Y. Guo, Application of an improved multi-conductor transmission line model in power transformer, IEEE Trans. Magn. 49 (5) (2013) 2029–2032.
[62] A. Baggini, C. Ploetner, J.C. Riboud, Functional definition and classification of the power transformer, IEEE Trans. Power Deliv. 38 (1) (2023) 80–84.
[63] M.G.S. Pearce, G.A. Covic, J.T. Boys, Robust ferrite-less double D topology for roadway IPT applications, IEEE Trans. Power Electron. 34 (7) (2019) 6062–6075.
[64] J.-W. Yeh, S.-K. Chen, S.-J. Lin, J.-Y. Gan, T.-S. Chin, T.-T. Shun, C.-H. Tsau, S.-Y. Chang, Nanostructured high-entropy alloys with multiple principal elements: novel alloy design concepts and outcomes, Adv. Eng. Mater. 6 (5) (2004) 299–303.
[65] Y. Zhang, T. Zuo, Y. Cheng, P.K. Liaw, High-entropy alloys with high saturation magnetization, electrical resistivity and malleability, Sci. Rep. 3 (1) (2013) 1455.
[66] V. Chaudhary, M.S.K.K.Y. Nartu, S. Dasari, S.M. Varahabhatla, A. Sharma, M. Radhakrishnan, S.A. Mantri, S. Gorsse, N.B. Dahotre, R.V. Ramanujan, R. Banerjee, Magnetic and mechanical properties of additively manufactured Alx (CoFeNi) complex concentrated alloys, Scripta Mater. 224 (2023) 115149.
[67] G. Herzer, Modern soft magnets: amorphous and nanocrystalline materials, Acta Mater. 61 (3) (2013) 718–734.
[68] D. Jiles, Introduction to Magnetism and Magnetic Materials, CRC Press, 2015.
[69] X. Liu, Y. Duan, X. Yang, L. Huang, M. Gao, T. Wang, Enhancement of magnetic properties in FeCoNiCr0.4CuX high entropy alloys through the cocktail effect for megahertz electromagnetic wave absorption, J. Alloys Compd. 872 (2021) 159602.
[70] Y. Duan, H. Pang, X. Wen, X. Zhang, T. Wang, Microwave absorption performance of FeCoNiAlCr0.9 alloy powders by adjusting the amount of process control agent, J. Mater. Sci. Technol. 77 (2021) 209–216.
[71] R. Aiswarya, E. Barnabas, R.S. Hari Shankar, S. Nandagopal, A.N. Archana, Design and simulation of wireless power transfer system for electric vehicle application, in: K. Namrata, N. Priyadarshi, R.C. Bansal, J. Kumar (Eds.), Smart Energy and Advancement in Power Technologies, Springer Nature Singapore, Singapore, 2023, pp. 363–374.
[72] M. Aishwarya, R.M. Brisilla, Design of Energy-Efficient Induction motor using ANSYS software, Results in Engineering 16 (2022) 100616.
[73] S. Viqar, A. Ahmad, S. Kirmani, Y. Rafat, M.R. Hussan, M.S. Alam, Modelling, simulation and hardware analysis of misalignment and compensation topologies of wireless power transfer for electric vehicle charging application, Sustainable Energy, Grids and Networks 38 (2024) 101285.
[74] T. Bouanou, H. El Fadil, A. Lassioui, I. Bentalhik, M. Koundi, S. El Jeilani, Design methodology and circuit analysis of wireless power transfer systems applied to electric vehicles wireless chargers, World Electric Vehicle Journal 14 (5) (2023) 117.
[75] M.A. Badwey, N.H. Abbasy, G.M. Eldallal, An efficient design of LC-compensated hybrid wireless power transfer system for electric vehicle charging applications, Alex. Eng. J. 61 (8) (2022) 6565–6580.
[76] S. Kuzey, S. Balci, N. Altin, Design and analysis of a wireless power transfer system with alignment errors for electrical vehicle applications, Int. J. Hydrogen Energy 42 (28) (2017) 17928–17939.
[77] A.L. Patterson, The scherrer formula for X-ray particle size determination, Phys. Rev. 56 (10) (1939) 978–982.
[78] V.D. Mote, Y. Purushotham, B.N. Dole, Williamson-Hall analysis in estimation of lattice strain in nanometer-sized ZnO particles, Journal of Theoretical and Applied Physics 6 (1) (2012) 6.
[79] F. Navarro-Pardo, G. Martínez-Barrera, A.L. Martínez-Hernández, V.M. Castaño, J. L. Rivera-Armenta, F. Medellín-Rodríguez, C. Velasco-Santos, Effects on the thermo-mechanical and crystallinity properties of nylon 6,6 electrospun fibres reinforced with one dimensional (1D) and two dimensional (2D) carbon, Materials (2013) 3494–3513.
[80] T. Matsushita, Current and Magnetic Flux Density, Electricity and Magnetism: New Formulation by Introduction of Superconductivity, 2014, pp. 123–154.
[81] C. Alexandru, D. Zhu, Limitations of Ansys-Maxwell and Simplorer Magnetostatic co-simulation in Inductive Wireless Power Transfer, 2022 Wireless Power Week (WPW) (2022) 818–823.